processes

MDPI

*Article*

# Model-Based Optimization of Multi-Stage Nanofiltration Using the Solution-Diffusion–Electromigration Model

**Tobias Hubach, Stefan Schlüter and Christoph Held ***

Laboratory of Fluid Separations, TU Dortmund University, Emil-Figge Str. 70, 44227 Dortmund, Germany; tobias.hubach@tu-dortmund.de (T.H.); stefan2.schlueter@tu-dortmund.de (S.S.)
* Correspondence: christoph.held@tu-dortmund.de; Tel.: +49-2317552086

**Abstract:** Nanofiltration is well suited to separate monovalent ions from multivalent ions, such as the separation of $Li^+$ and $Mg^{2+}$ from seawater, a potential lithium source for the production of lithium-ion batteries. To the best of our knowledge, there is no existing work on the optimization of a multi-stage membrane plant that differentiates between different ions and that is based on a validated transport model. This study presents a method for modeling predefined membrane interconnections using discretization along the membrane length and across the membrane thickness. The solution-diffusion–electromigration model was used as the transport model in a fundamental membrane flowsheet, and the model was employed to optimize a given flowsheet with a flexible objective function. The methodology was evaluated for three distinct separation tasks, and optimized operating points were found. These show that permeances and feed concentrations might cause negative rejections and positive rejections (especially for bivalent ions) depending on the ions' properties and fluxes, thereby allowing for a favorable separation between the ions of different valence at optimized conditions. In an application-based case study for the separation of $Li^+$ and $Mg^{2+}$ from seawater, the method showed that under optimal conditions, the mol-based ratio of $Mg^{2+}/Li^+$ can be reduced from 2383 to 2.8 in three membrane stages.

**Keywords:** membrane separation; solution-diffusion–electromigration; process design; modeling; optimization; ion permeances; lithium; magnesium



**Citation:** Hubach, T.; Schlüter, S.; Held, C. Model-Based Optimization of Multi-Stage Nanofiltration Using the Solution-Diffusion–Electromigration Model. *Processes* **2023**, *11*, 2355. https://doi.org/10.3390/pr11082355

Academic Editor: Liliana C. Tomé

Received: 14 July 2023
Revised: 26 July 2023
Accepted: 2 August 2023
Published: 4 August 2023



## 1. Introduction

Nanofiltration allows separating monovalent ions from multivalent ions. Hence, nanofiltration might be applied to the separation of $Li^+$ and $Mg^{2+}$ ions from seawater. This is of interest since seawater is by far the largest source (~230 billion tons) for these ions on Earth [1,2]. In the fabrication steps of lithium-ion batteries, the ratio of $Mg^{2+}/Li^+$ should be as low as possible to minimize the use of sodium carbonate to precipitate $Mg^{2+}$ [3]. However, the mass-based $Mg^{2+}/Li^+$ ratio in seawater is about 8500 [4]. Thus, a suitable separation process is necessary to achieve much lower ratios. At ratios below 6, the purification steps from the conventional lithium purification method can be combined with membrane separation [5,6]. Through coupling with the increasingly relevant reverse osmosis systems, nanofiltration can represent a promising process to separate $Li^+$ and $Mg^{2+}$ ions from seawater and other aqueous sources such as salt lakes. Such complex hybrid processes require optimized designs provided by reliable transport models that are predictive or, at least, extrapolative. However, to the best of our knowledge, a purely predictive physical model does not exist for nanofiltration. This is probably due to the particularly complex interaction behavior caused by different phenomena and interactions between charged solutes and the membrane. In addition to size exclusion, the Donnan effect and the dielectric exclusion effect play a role in electrolyte separation [7]. The Donnan effect is caused by the mostly negative charge on the membrane surface, which leads to an electric potential difference (the so-called Donnan

potential) at the membrane–feed interface. Thus, the counter ions are rejected due to electrostatic repulsion. Concomitantly, to maintain the solution's electroneutrality, the co-ion is repelled [8]. Dielectric exclusion occurs because the dielectric constant in the bulk solution differs from that in the membrane pores. Mirror charges induced by this difference lead to a higher rejection, especially for divalent ions [9]. Nevertheless, there are models to describe aqueous nanofiltration, such as the Spiegler–Kedem transport model [10], Teorrell–Meyer–Sievers model [11] and the Donnan–steric-pore–dielectric exclusion model (DSPM-DE) [12]. The latter has been applied for different nanofiltration applications, such as the separation of NaCl /$Na_2SO_4$ [13], the purification of amine solutions [14], and the prediction of rejection of various single salt solutions [15]. Wang and Lin [16] stated that the DSPM-DE model requires excessive experiments and lacks in prediction performance. The different models in nanofiltration were summarized recently in the works of Bandini and Boi [17] and Yaroshchuk et al. [18]. These models require a set of parameters to characterize the nanopores (if present). In contrast, Yaroshchuk et al. [18–20] introduced the so-called solution-diffusion–electromigration model (SDEM) which is based on the assumption of virtual solutions, defined to be in thermodynamic equilibrium with an infinitely small volume of the membrane. It is an extension of the classical solution-diffusion model and assumes that there is no convective coupling between transmembrane volume flux and solute transport. Consequently, only one phenomenological parameter, the ion permeance, is required by the SDEM to describe the ion transport within a membrane. These ion permeances also account for the important relation between different transmembrane ion fluxes via spontaneously arising electric field. Unlike the Spiegler–Kedem and solution diffusion model, it is also possible to accurately model low and negative rejections. A detailed description of the derivation of the model as well as application examples can be found in the works of Yaroshchuk et al. [19,20]. Recently, research groups have started to apply the SDEM [21,22], e.g., Labastida and Yaroshchuk [21] used the SDEM model to fit ion permeances to experimental data obtained by a rotating disk-like membrane in order to study the effect of concentration polarization. Recently, the model was extended by López et al. [22], who also considered the formation of the $MgSO_4$ ion pairs resulting from an equilibrium dissociation reaction and determined a permeance for the ion pair species as well. However, the relationship between ion rejection and permeate flux was not significantly affected by this extension of the model.

Besides the above-described local flux models, an optimization model for multistage membrane separation is required to design complex membrane plants. Several works with different levels of complexity exist in the literature on the optimized design of membrane plants, especially for reverse osmosis. While some works even consider the hydrodynamics in the membrane cell [23], most of the published works treat mass transfer in a very simplified way [24]. Skiborowski et al. [24] developed a superstructure to optimize a reverse osmosis process by simultaneously considering the operating parameters and process structure. However, the presence of different ions or of an electric field in the membrane were not accounted for in the applied solution-diffusion model. Furthermore, Kotb et al. [25] optimized various arrangements of a reverse osmosis plant by minimizing total cost per volume flow of permeate. In addition to the simplified solution-diffusion model (SDM) with one parameter for salt and one for water, the concentration polarization was also taken into account using film theory [25]. A multi-objective optimization for membrane networks in seawater desalination was proposed by Du et al. [23]. They mainly evaluated pressure loss in the membrane module as well as the process economics by suggesting different energy recovery options.

The literature on optimization and designs of nanofiltration processes is scarce. Garg and Joshi [26] performed an optimization and techno-economic analysis for nanofiltration and reverse osmosis. The model was obtained by response surface methodology. Here, the relationships between several explanatory variables (temperature, pressure, and concentration) and one or more response variables (rejection, energy consumption) were examined

and regressed. A similar approach was taken by Alves et al. [27] who found the optimal transmembrane pressure and temperature for the purification of xylitol using the surface response methodology. However, instead of ion rejections, only total salt rejection was considered and optimization was limited to a small-scale membrane system with a membrane area of 0.015 $m^2$. Geralded and Alves [28] developed a computer program to model solute transport in nanofiltration membranes using the Donnan steric partitioning pore and dielectric exclusion model (DSPM-DE) with incorporation of electrolyte solution non-ideality and concentration polarization effects. Although the local flux was considered in detail, process optimization, multi-stage processes, or changes along the membrane length were not considered. The latter was taken up by Roy et al. [29] who also used the DSPM-DE to simulate nanofiltration modules with flat-sheet and spiral-wound leaves to investigate the influence of various operating parameters on the performance. The modules were divided into segments to account for pressure drop and varying solute concentration. However, mathematical optimization and interconnection of these modules were not investigated.

Therefore, in this work, we demonstrate the modeling of multi-stage membrane separations by means of the sophisticated SDEM with permeances obtained from simple lab experiments. Thus, for the first time, the SDEM is applied in the discretization along the module length of a membrane stage to account for changing conditions (i.e., pressure and concentration). In addition, the pressure drop was taken into account to model the reduced driving force along the module. Computation time was kept low by transforming the set of differential and algebraic equations into a fully algebraic system of equations and using an advanced initialization strategy. In particular, the SDEM model is used for the first time to optimize operating conditions such as pressure and membrane area. Furthermore, a multi-stage membrane process is proposed and calculated for the first time for the important separation task $Li^+/Mg^{2+}$. The model equations, solution, and initialization methods are presented in Section 2, followed by their application in three case studies in Section 3. Both a hypothetic test mixture and two real mixtures with experimental data were used as case studies. The resulting process configurations were discussed regarding the membrane module connections and dominant transport effects.

## 2. Computational Methods

While most models for multi-ionic solutions contain a large number of parameters, Yaroshchuk et al. [20] were able to develop a model with only one adjustable parameter per ion, namely the single-ion permeance $P_i$ (cf. Equation (1)). It is important to note that the model neglects the convective coupling between trans-membrane volume flux of the solvent (usually water) and solute flux. Derived from the SDEM of Yaroshchuk et al. [20], the definition of the electrochemical potential and setting activity coefficients equal to 1 across the membrane, $n$ equations of the following form were obtained ($n$ represents the number of different ions in the solution) to describe the molar solute flux $j_i$ of ion $i$ through a membrane:

$$j_i = -P_i \frac{dc_i}{dx} - c_i P_i Z_i \frac{F}{RT} \frac{d\phi}{dx} \quad (1)$$

In Equation (1), $c_i$ is the ion concentration in the virtual solution, $x$ is the transmembrane coordinate, $z_i$ is the ion charge, $F$ is the Faraday constant, and $\phi$ the electrostatic potential. $P_i$ is the product of local diffusion and partition coefficients, where the partition coefficient is the ratio of concentrations in the real and virtual solutions. In principle, $P_i$ is not constant but a function of position and concentration. For simplicity, we assumed $P_i$ to be constant across the membrane, which in turn implies that the local partition coefficient does not change across the membrane. This assumption was also made by Yaroshchuk [19] and Fridman-Bishop [30]. In addition to the flux equations, the electroneutrality condition (cf. Equation (2)) has to be fulfilled in every point of the virtual solution.

$$\sum_{i=1}^{n} c_i \cdot Z_i = 0 \quad (2)$$

### *2.1. Orthogonal Collocation*

Orthogonal collocation is a numerical method to solve differential equations and differential-algebraic equations considering boundary conditions by transforming the set of equations into purely algebraic equations. Yaroshchuk and Bruening [9] developed analytical solutions for special applications, which enable a fast and simple calculation of the flux and concentration profile. However, analytical solutions are restricted to a small number of ion species. In order to solve the differential-algebraic equation system in a general way, we transformed the Equations (1) and (2) into an algebraic system of equations using orthogonal collocation, which can be solved by any non-linear programming solver. We used $v = 6$ collocation points, four internal collocation points, and one at $z_0 = 0$ and one at $z_v = 1$. Note that $z$ is the dimensionless transmembrane coordinate $z = \frac{x}{\delta}$. Thus, the boundary conditions were taken into account when solving the system of Equations (1) and (2). The first boundary condition at $z_0 = 0$ describes the feed concentration of the components in the respective node. The second boundary condition results from the relationship between ion concentration in the permeate $c_i^P$, ion flux $j_i$ and the total permeate volume flux $J_v$:

$$j_i = c_i^P \cdot J_v \tag{3}$$

To solve Equations (1) and (2), the concentration profile of an ion and the electrostatic potential over the membrane thickness $\delta$, so-called modelled variables $y$, were approximated using polynomials $y(z)$ with coefficients $\alpha_i$:

$$y(z) = \theta_0 + \theta_1 z + \theta_2 z^2 + \ldots + \theta_v z^v \tag{4}$$

Thus, for a polynomial of degree $v$, $v$ collocation points were set across the thickness of the membrane. In this work, the collocation points were not chosen equidistantly, but result from the roots of the shifted Lagrange polynomials. The equation system can be solved by forming the derivatives of Equation (4), mathematically transforming and inserting it into Equations (1) and (2). A detailed description can be found in our previous paper [31].

### *2.2. Model Development*

A tool was developed in this work to solve and optimize a steady-state multi-stage membrane process in order to use the SDEM also for engineering applications. To account for the changes in fluxes, ion concentrations, and feed pressures along the membrane length in each stage, the membrane was axially discretized. That is, "feed" relates to the inlet into each node, and thus, ion concentrations and pressure vary from node to node. Figure 1 schematically depicts the structure of a membrane stage consisting of $N$ nodes elements connected in series. Thus, the retentate flow rate of the $j$-th node is the feed flow rate into the $j + 1$-th node. This is analogous to the concentrations of the feed and retentate stages. The permeate streams from each node were virtually combined in a mixing point to the final permeate stream.

In each node, the ion flux was obtained by solving Equations (1)–(3). The total permeate flux $J_v^j$ in the node $j$ is given here by the permeability $Q_{H_2O}$ of salt water, the feed pressure $p^F$ supplied by the pump, the permeate pressure $p^P$ the osmotic pressure difference $\pi^{j,F} - \pi^{j,P}$, and the pressure loss within the node $\Delta p_f^j$ according to Equation (10):

$$J_v^j = Q_{H_2O} \cdot \left( p^F - p^P - \left( \pi^{j,F} - \pi^{j,P} \right) - \Delta p_f^j \right) \tag{5}$$

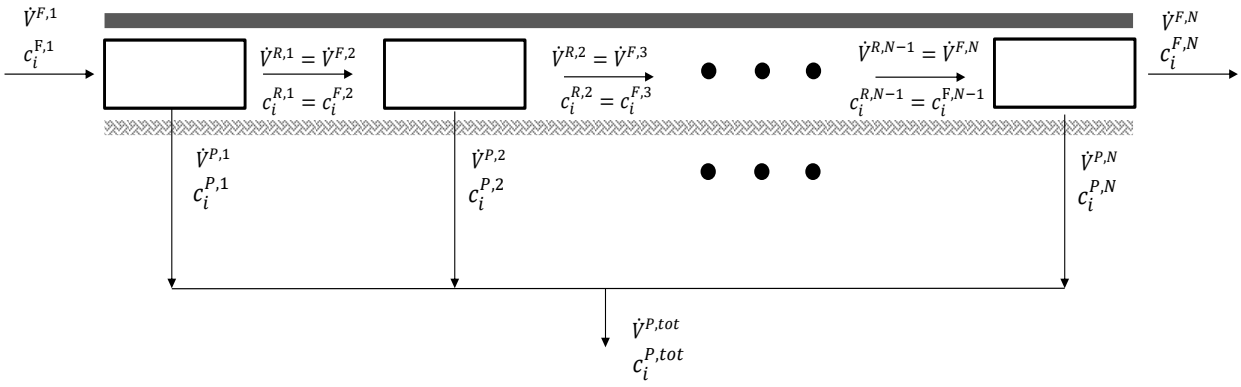


**Figure 1.** Membrane discretization scheme with $N$ nodes. The feed variables denote the inlet states into the respective node, i.e., the feed pressure and the feed concentrations vary from node to node.

The calculation of the pressure drop $\Delta p_f^j$ in every node of a tube module is presented in Supplementary Materials S1. The pressure loss between the stages was neglected [25]. The osmotic pressures in the permeate $\pi^P$ and in the feed $\pi^F$ were calculated in a simplified way using Van 't Hoff equation for dilute solutions [16,17]:

$$\pi_{F/P}^j = RT \cdot \sum_{i=1}^{N} c_{iF/P}^j \tag{6}$$

In a single node $j$, all streams were distinctly determined by the mass balance (assuming no excess volume) and component balance according to Equations (7) and (8):

$$c_i^{j,F} \cdot \dot{V}^{F,j} = c_i^{j,F} \cdot \dot{V}^{P,j} + c_i^{j,R} \cdot \dot{V}^{R,j} \tag{7}$$

$$\dot{V}^{F,j} = \dot{V}^{P,j} + \dot{V}^{R,j} \tag{8}$$

The flux model was solved in all nodes in parallel. To enable interconnection from multiple membrane modules, the retentate or permeate streams from the first stage were then connected to a second membrane stage to provide a permeate or retentate concentration.

Note that the stage-cut, i.e., the ratio of permeate-to-feed volume stream was specified in advance for each stage. The modeling problem was first solved for a small number of membrane nodes using the Matlab™ solver *fmincon* with a sequential quadratic programming algorithm (SQP). Solving this reduced problem with significantly fewer variables yielded initial values for simulating the problem with more nodes. Figure S1 depicts a flowchart of the calculation algorithm. All computations have been performed on a PC with an AMD Ryzen 7 5700 U CPU.

For the three case studies conducted in this study, the constraints and objective functions used are listed in the respective Sections 3.1–3.3 to increase readability and understanding of the study.

### *2.3. Optimization*

The presented process model was additionally subjected to optimization with respect to different target objective functions. Possible objective functions are for instance the rejection of a specific component $R_i$, the recovery of a component $Rec_i$, or the membrane area to fulfil a specific separation task. The nonlinear constraints to be fulfilled are given by Equations (1)–(3), (5)–(8) and (S1)–(S6). Finally, the optimization gave the feed pressure in every stage to fulfil the separation task as it can be supplied by pumps and the necessary

membrane area. The ion rejection $R_i$, the recovery of a component $Rec_i^P$ in the permeate, and the separation factor $SF_{i,k}$ of an entire stage are defined as follows:

$$R_i = 1 - \frac{c_i^P}{c_i^F} \tag{9}$$

$$SF_{i,k} = \frac{\frac{c_i^F}{c_k^F}}{\frac{c_i^P}{c_k^P}} \tag{10}$$

$$Rec_i^P = \frac{c_i^P \cdot \dot{V}^P}{c_i^F \cdot \dot{V}^F} \tag{11}$$

A full list of the variables can be found in Table S1 in the Supplementary Materials. In this study, our focus was primarily on the fundamental aspects of our modeling and optimization approach, namely the transport model and operating conditions. We made a conscious decision not to extend the optimization to include costs due to their inherent uncertainty and the common practice among companies to utilize custom cost parameter matrices. Nevertheless, it is worth noting that incorporating additional functions into our framework can be easily achieved without significant effort, providing potential avenues for future extensions.

## 3. Results

The performance of the optimization approach presented in Section 2.3 was evaluated by three case studies. In the first case study, Section 3.1, published ion permeances were used to simulate and optimize a multi-stage nanofiltration process for a system with three ions. In the second case study, Section 3.2, ion permeances were fitted to experimental flux data for a system with four ions. In contrast to the first case study, the membrane area for a given separation task served as the target function to be minimized. In a third case study, the focus was placed specifically on the separation of $Li^+$ and $Mg^{2+}$ from an aqueous stream. Here, the permeances used were derived from experimental data as well.

### 3.1. Case Study 1—Modeling and Optimization of a Hypothetic Mixture

The proposed methodology for nanofiltration system optimization was applied to investigate the operational characteristics of a multi-stage nanofiltration system of a hypothetical multi-electrolyte mixture in order to separate the ions $A^-$ and $B^{2-}$ of the two salts MA and $M_2B$. By using an analytical solution of the SDEM model, Yaroshchuk and Bruening [19] predicted the behavior of the ion rejections versus the permeate flux $J_v$. The ion permeances [19] and other parameters used in this case study are listed in Tables S2–S4.

A three-stage process was simulated with the parameters from Table S2 according to the model scheme in Section 2.2. As an additional condition, it was specified that the permeate flow of a stage corresponds to 25% of the feed flow of the respective stage, the so-called stage-cut. With a fixed feed pressure, a lower stage cut would result in a smaller membrane and vice versa. The supplied pump pressure was set to 8 bar in all stages. Further, the seawater permeance was set in this work, as it was not specified in the original work from Yaroshchuk and Bruening [19], which is why the pressure could not be re-converted from Yaroshchuk and Bruening [19] and thus, was set to 8 bar. Due to the fixed pump pressure and permeance, the permeate flux results directly from Equation (10).

Nevertheless, the ion feed concentrations and the temperature were inherited also from Yaroshchuk and Bruening [19], and thus, only the number of nodes and the stage-cut and saltwater permeance were set to fixed input value in this case study.

Figure 2 presents the resulting process flow diagram with all relevant flows and concentrations of the three ions $A^-$, $B^{2-}$, and $M^+$. Due to the constant pump pressure at the feed of all stages, the area of the membrane stages decreases according to the stage-cut.

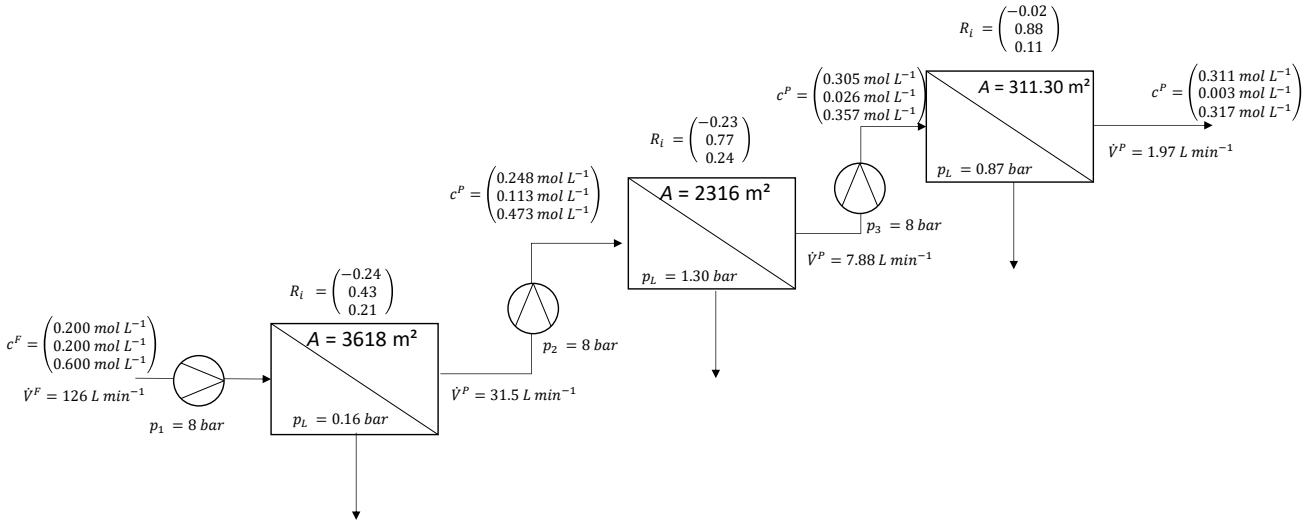


**Figure 2.** Modeled three-stage membrane flowsheet of case study 1 with fixed pump pressure in each stage ($p_{pump}$ = 8 bar) including parameters of Tables S2 and S3. Ion concentrations and rejections in the $c_i$ and $R_i$ vector are in the order $A^-$, $B^{2-}$, and $M^+$.

Figure 3 shows the calculated ion rejections in the first node of each stage as a function of the total permeate flux for the corresponding feed concentrations. Interestingly, the ion rejections differ from stage to stage. The divalent ion $B^{2-}$ has the lowest permeance of the ions and thus shows the highest rejection. The monovalent anion $A^-$ exhibits a negative rejection at low permeate fluxes, which changes to a positive rejection for higher permeate fluxes. This might be caused by spontaneous electric fields that accelerate the permeation of $A^-$ to ensure a net-zero current. Moreover, the feed concentration of $B^{2-}$ decreases from stage to stage (cf. Figure 3b,c), and negative rejection of $A^-$ no longer occurs. This indicates that the concentration of $B^{2-}$ is crucial for the occurrence of accelerating/deaccelerating electric fields and negative rejections [19].

The vertical lines in Figure 3 show the operating points simply resulting from the specified pressure and the given saltwater permeance. Note, these input settings were not optimized but arbitrarily chosen in this work. Recognizably, these operating points are not the operation conditions of optimal separation performance, which would occur at the maximum distance of the rejection curves of $A^-$ vs. $B^{2-}$. Hence, there is huge potential for more effective separation by shifting the operating point towards higher fluxes. The separation factors between component $A^-$ and $B^{2-}$ at the operating points are 3.7 (stage 1), 2.8 (stage 2), and 3.9 (stage 3), respectively.

Achieving a more effective separation of $A^-$ from $B^{2-}$ might also be possible by optimization. Thus, an objective function was defined within the SDEM to maximize the difference between the rejections of ions $A^-$ and $B^{2-}$:

$$obj = \left(1 - \frac{c^P_{A^-}}{c^F_{A^-}} - 1 - \frac{c^P_{B^{2-}}}{c^F_{B^{2-}}}\right) \tag{12}$$

Figure 4 illustrates the optimized three-stage membrane process with modeled ion concentrations, ion rejections, and fluxes in each of the three stages. The separation factors for the separation of ions $A^-$ from $B^{2-}$ were increased to 13.95 (stage 1), 8.34 (stage 2), and 12.87 (stage 3), respectively. In comparison to the modeling with constant pump pressures, this is an increase of greater than 300%.

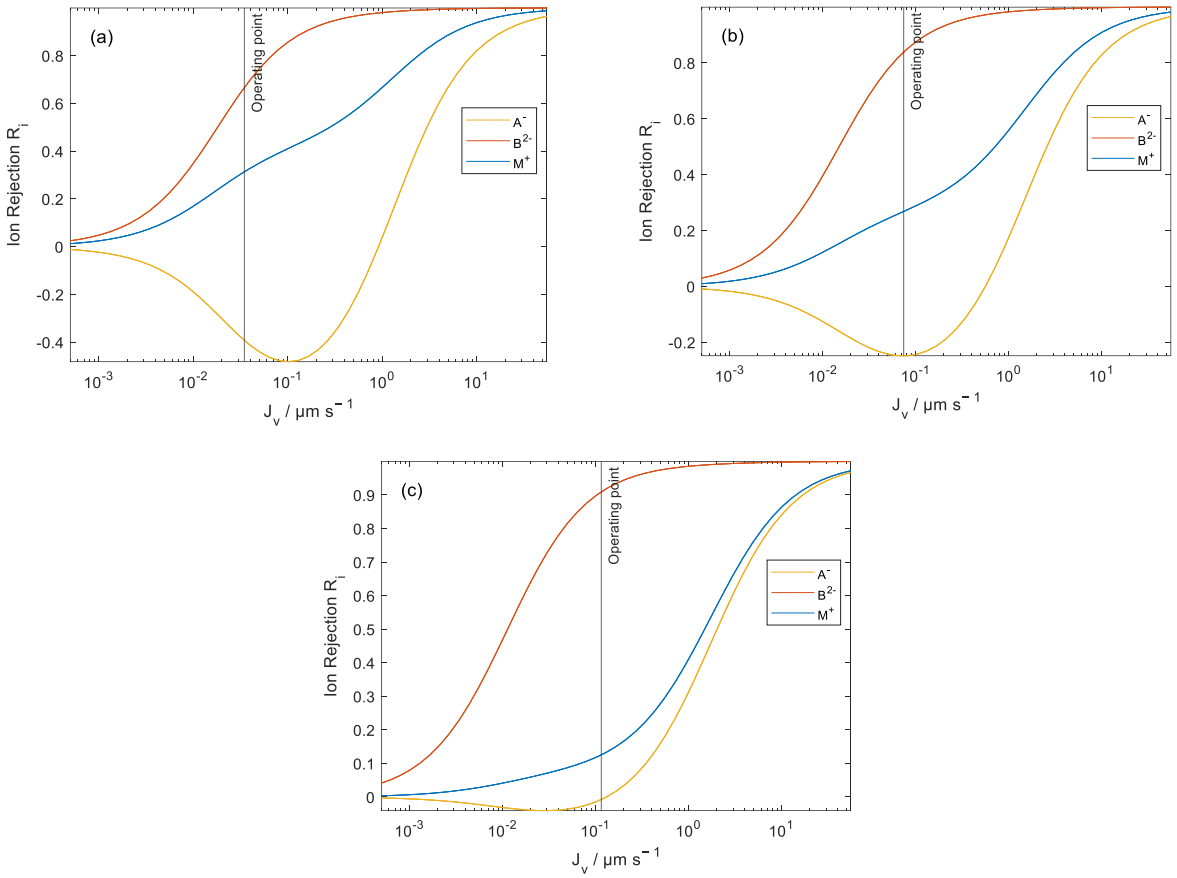


**Figure 3.** Ion rejections of three membrane stages as a function of the total permeate flux calculated by the SDEM model and operating point at fixed pump pressure ($p_{pump}$ = 8 bar) with parameters of Tables S2 and S3. Calculated rejections of ion species $A^-$ are depicted in yellow, $B^{2-}$ in red, and $M^+$ in blue. (**a**) corresponds to the first node in the first membrane stage and (**b**,**c**) to the second and third membrane stage, respectively.

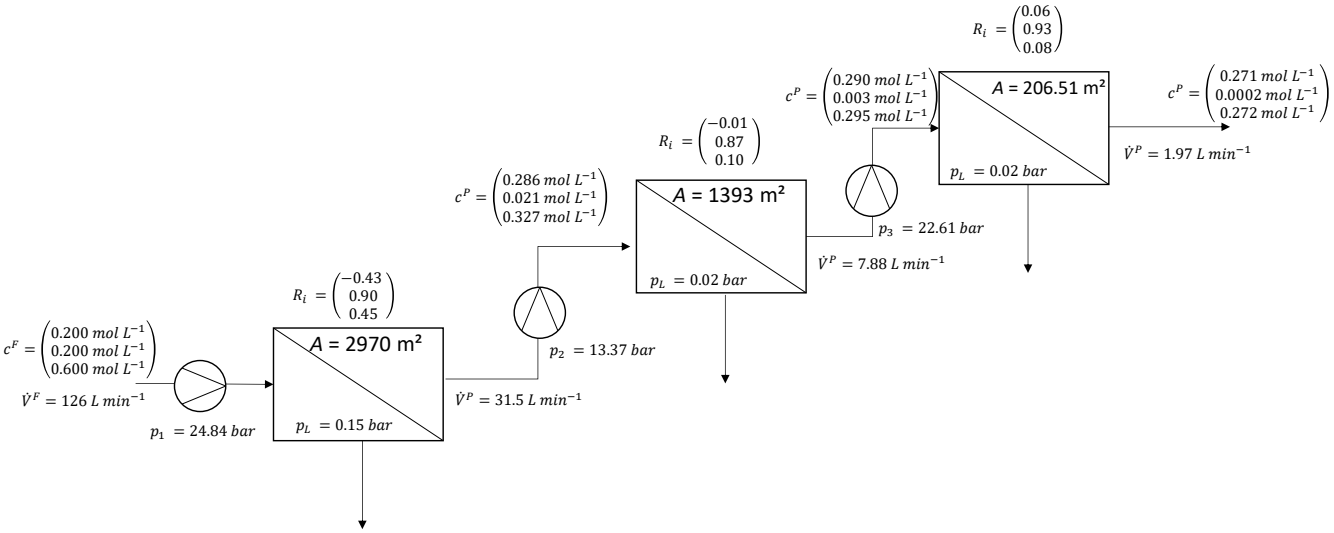


**Figure 4.** Optimized three-stage membrane flowsheet of case study 1 with optimized pump pressure in each stage with parameters of Tables S2 and S4. Ion concentrations and rejections in the $c_i$ and $R_i$ vector are in the order $A^-$, $B^{2-}$, and $M^+$.

A more detailed picture of this result is given in the following. Figure 5 shows the calculated ion rejections in the first node of each stage as a function of the total permeate flux for the optimized flowsheet in Figure 4. The computational time including the initialization was 104.04 s with 1019 variables to be computed. By the applied optimization, the operating point, marked in Figure 5 as a vertical line, is shifted to the right to higher permeate fluxes, thereby maximizing the separation of the ions $A^-$ and $B^2$. However, the operating and investment costs at the optimized operating point in Figure 5 will change (compared to Figure 2 setup) caused by the smaller membrane area and the higher required pressure. If the operating point were at the minimum of $A^-$ in Figure 5, the concentration of $A^-$ in the permeate would become maximum, but the separation of $A^-$ and $B^{2-}$ would not, due to the significantly lower rejection of $B^{2-}$.

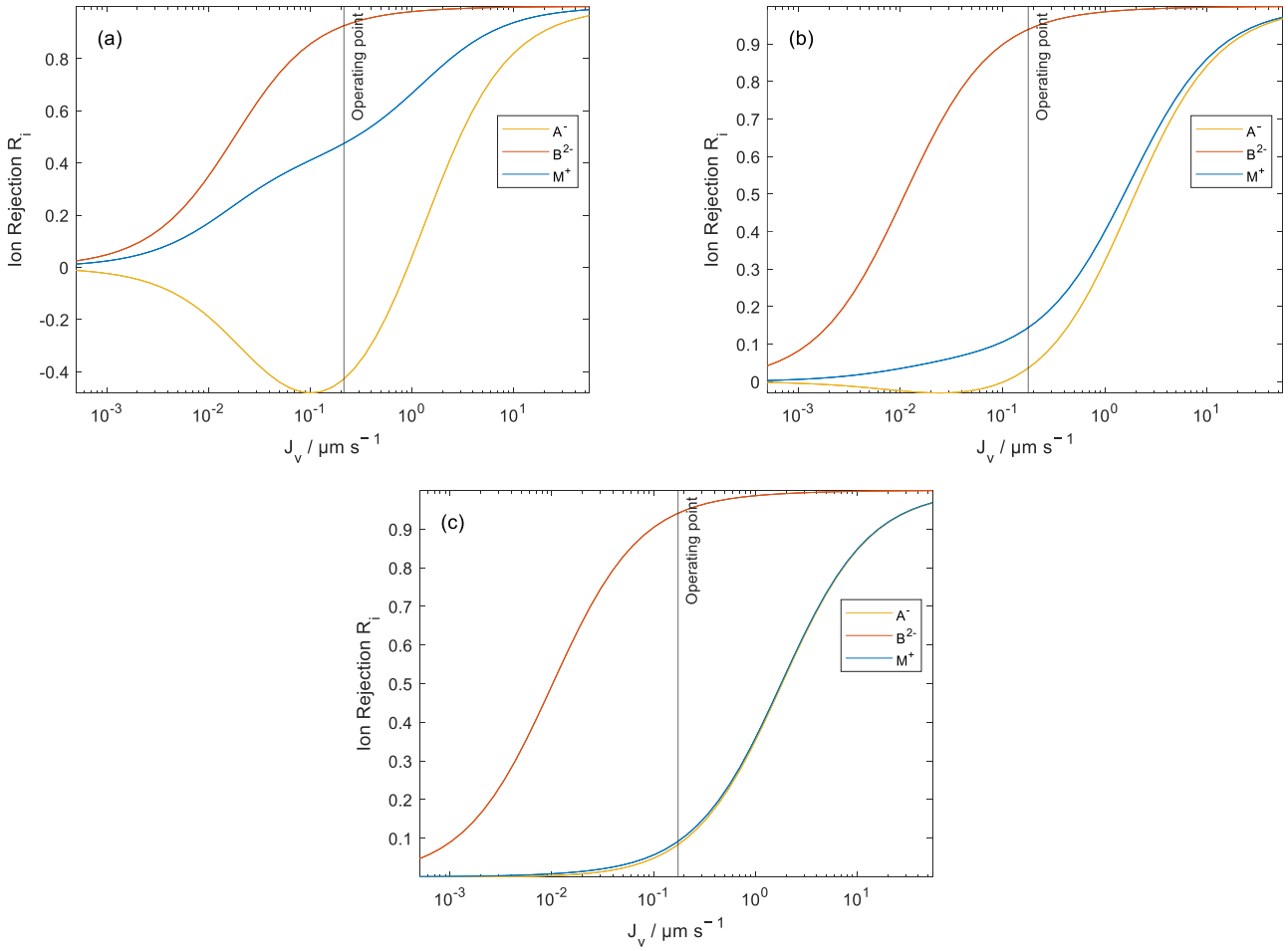


**Figure 5.** Ion rejections of three membrane stages as a function of the total permeate flux calculated by the SDEM model and operating point at optimized pump pressure with parameters of Tables S2 and S4. Calculated rejections of ion species $A^-$ are depicted in yellow, $B^{2-}$ in red, and $M^+$ in blue. (**a**) corresponds to the first membrane stage and (**b**,**c**) to the second and third membrane stage, respectively.

A more detailed insight is provided in Figure 6a illustrating the variation of the concentrations over the dimensionless membrane coordinate for the first node in the first membrane stage. The ions $B^{2-}$ and $M^+$ show a positive rejection (negative slope) with high concentration gradients. In contrast, concentration of $A^-$ increases over the coordinate resulting in negative rejection (concentration of $A^-$ in the permeate is higher than at the feed side). This is caused by the mass transport against the concentration gradient due to the attraction of anions by the electric field. The considerable increase in the concentration of $A^-$ at the end of the membrane might be explained by the electrostatic potential gradient,

cf. Figure 6a. Due to the significant increase in the electric field gradient at the end of the membrane, these ions are accelerated significantly towards the permeate side. Vice versa, $M^+$ is decelerated because of its positive charge.

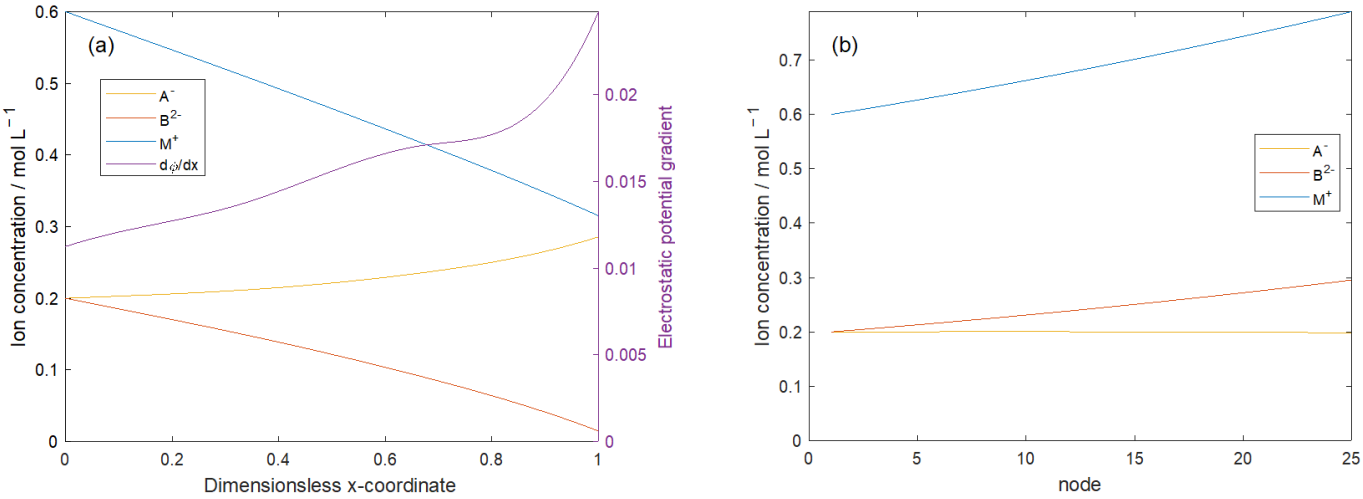


**Figure 6.** Transmembrane ion concentrations of the virtual solution in the first stage and first node of case study 1 (**a**) and feed concentrations as a function of membrane node in the first membrane stage (**b**) with parameters of Tables S2 and S3. Calculated concentrations of ion species $A^-$ are depicted in yellow, $B^{2-}$ in red, and $M^+$ in blue.

The concentration profile of the retentate stream along the membrane length is shown in Figure 6b for the 25 membrane nodes. $A^-$ shows a negative rejection (approx. −43% over the length) with constant slope, while non-linear effects occur for $B^{2-}$ and $M^+$ over the membrane coordinate. Counterintuitively, the concentration of $M^+$ increases more strongly than of $B^{2-}$, which might be due to the higher concentration of $M^+$ in the feed.

To sum up, this case study showed that the relationship between permeate flux and ion retention can be optimized with respect to the operating conditions (here: the pump pressure). The developed model is successful independent of the number of ion species. The used method revealed important information about the multistage membrane process. Instead of considering a single constant feed concentration, the entire process is considered. The separation did not appear as promising as it did for the initial concentrations in the first node and in the first stage. This result must be taken into account when selecting membranes for an industrial process, since the model only requires a few parameters and the expense of multiple membrane stages may therefore be justified.

### *3.2. Case Study 2—Modeling and Optimization of a Real Mixture*

In the second case study, the developed method was applied to experimentally obtained rejection data of a real mixture. For this purpose, a mixture of water, $MgSO_4$, and a trace salt NaI was considered. This system was investigated by Pages et al. [32] in a series of experiments of different dominant and trace salts. The membrane they used was an NF270 (Dow Chemical) with an active layer of semi-aromatic poly(piperazine). The ion rejections were obtained at transmembrane pressure differences between 4.5 bar and 20 bar at a constant temperature of 23 °C. We performed a regression to determine the ion permeances from the differential-algebraic equation system from Equations (1)–(3) for various total permeate fluxes $J_v$ using the experimental rejection data from Pages et al. [32] (cf. Table S5). The so-determined ion permeances and the average deviations of experimental and fitted ion rejections are listed in Table S6 at the feed concentration as given by Pages et al. [32]. Note that saltwater permeance and number of nodes were set to fixed values in this work. The result of the parameter regression is depicted in Figure 7, which illustrates the calculated ion rejections. These calculations were performed for different total permeate fluxes at the

experimental rejection data using the conditions and parameters listed in Tables S6 and S7. Thus, the calculated course also corresponds to the relationship between $J_v$ and $R_i$ in the first node of the first stage of the membrane structure. $Mg^{2+}$ and $SO_4^{2-}$ already show high rejections of more than 95% even at low permeate fluxes. Due to the significantly higher concentrations of $Mg^{2+}$ and $SO_4^{2-}$ compared to $Na^+$ and $I^-$, these rejections are also almost equal due to the electroneutrality condition in the solution. The $Na^+$ rejection also increases with increasing permeate flux but is clearly lower than the rejection of $Mg^{2+}$ and $SO_4^{2-}$. The rejection of $I^-$ is consistently negative, especially at small permeate fluxes. Spontaneously arising electric fields to ensure zero net current accelerate $I^-$ ions and enable ion transport through the membrane against the concentration gradient. The SDEM can reflect these data well with the regressed parameters, except for a slight deviation for $I^-$ at higher transmembrane volume fluxes. Thus, the obtained model can be used for further process design and membrane stage optimization.

In the flowsheet optimization of the second case study, we took a different approach by defining the membrane area as the objective function to be minimized. The stage cut was then treated as a free variable, and additional constraints were established to ensure proper separation in each stage. In the first stage, the requirement was set to recover a minimum of 50% of species $I^-$ in the permeate. For the second stage, specific conditions were chosen to limit the presence of $Mg^{2+}$ in the permeate to a maximum of 6% relative to the feed, to ensure that at least 27% of $I^-$ was present in the permeate, and to maintain a minimum $I^-$ concentration of $0.4 \cdot 10^{-3}$ mol $L^{-1}$ in the permeate. These constraints were arbitrarily set to demonstrate the range of possibilities achievable through this model-based optimization approach. For the optimized flowsheet for this case study, refer to Figure 8 The computational time including the initialization was 137.03 s with 1220 variables to be computed.

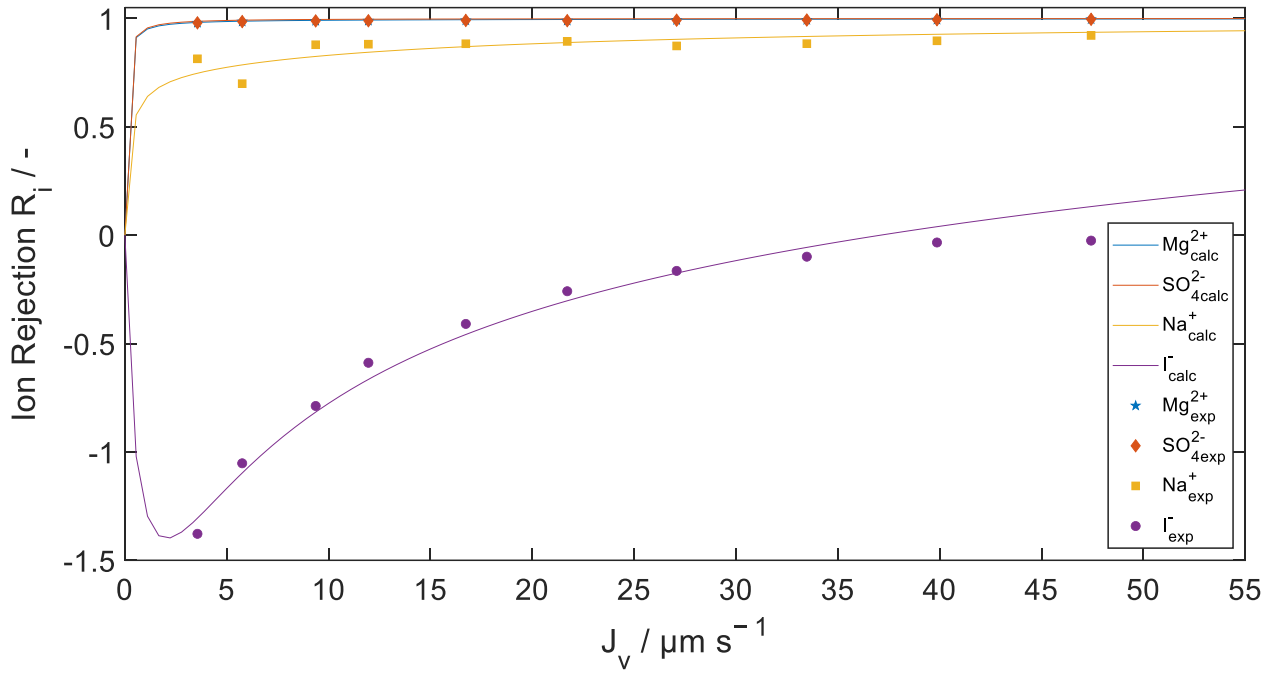


**Figure 7.** Experimental rejections (symbols) of $MgSO_4$ and NaI with NF270 at 23 °C at transmembrane pressure difference 7–20 bar from Pages et al. [32] and fitted rejections (solid lines) to the SDEM model using Equations (1) and (2). All experimental data points are listed in Table S5. $Mg^{2+}$ rejections are depicted in blue (★), $SO_4^{2-}$ in orange (♦), $Na^+$ in yellow (■), and $I^-$ in violet (●), whereby the blue symbol and blue line lay on the same positions as the orange ones.

Our model allows considering the changes in the rejection courses in further nodes as the model explicitly accounts for the dependence on the feed concentrations into the nodes. The changes over the nodes are illustrated in Figure 9, showing the relation between $J_v$ and ion rejections for chosen membrane nodes. The minimum $I^-$ rejection is even more pronounced in later nodes, caused by the increased concentration of divalent $Mg^{2+}$ ions, while the rejections of the other three ion species ($Na^+$, $Mg^{2+}$, $SO_4{}^{2-}$) do not differ significantly at the different nodes. It should be noted that the rejection of the entire first stage is $R_{I^-} = -0.929$, although the rejection of $I^-$ is $R_{I^-} < -1$ in each node of the first stage. This is the result of the feed concentration of the first node and the merged permeate streams.

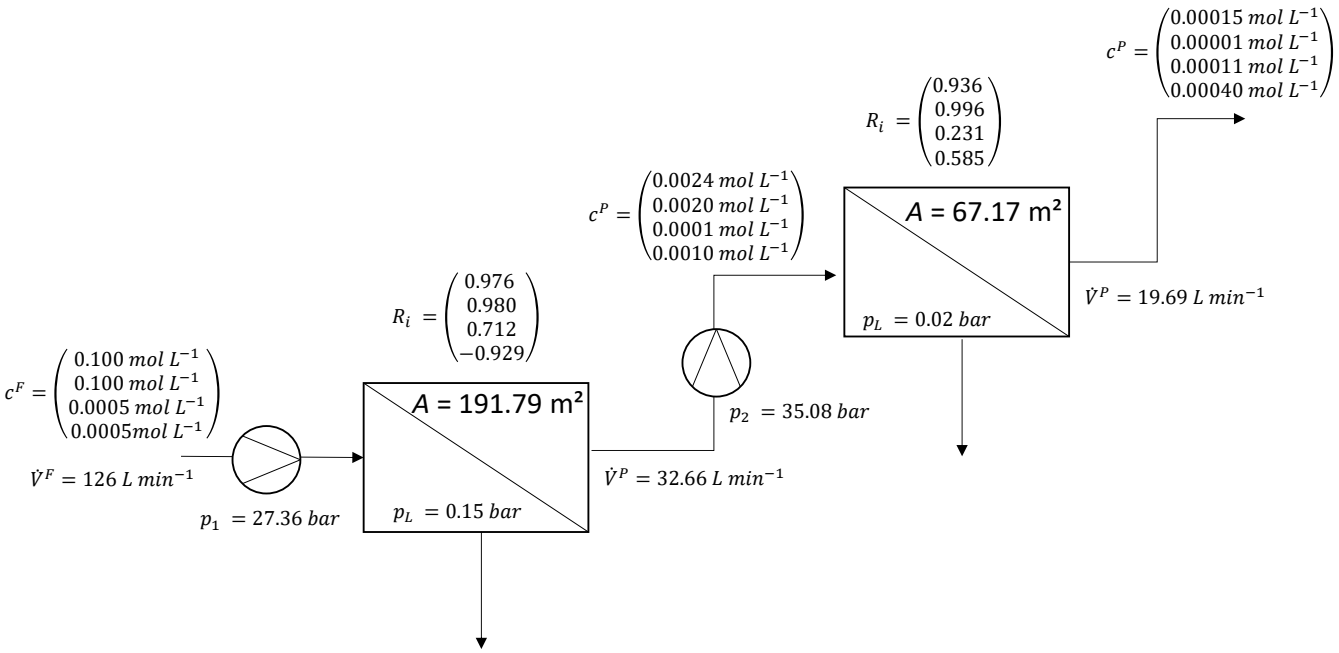


**Figure 8.** Optimized two-stage membrane flowsheet of case study 2 with optimized pump pressure in each stage including parameters of Tables S6 and S7. Ion concentrations and rejections in the $c_i$ and $R_i$ vector are in the order $Mg^{2+}$, $SO_4{}^{2-}$, $Na^+$, $I^-$.

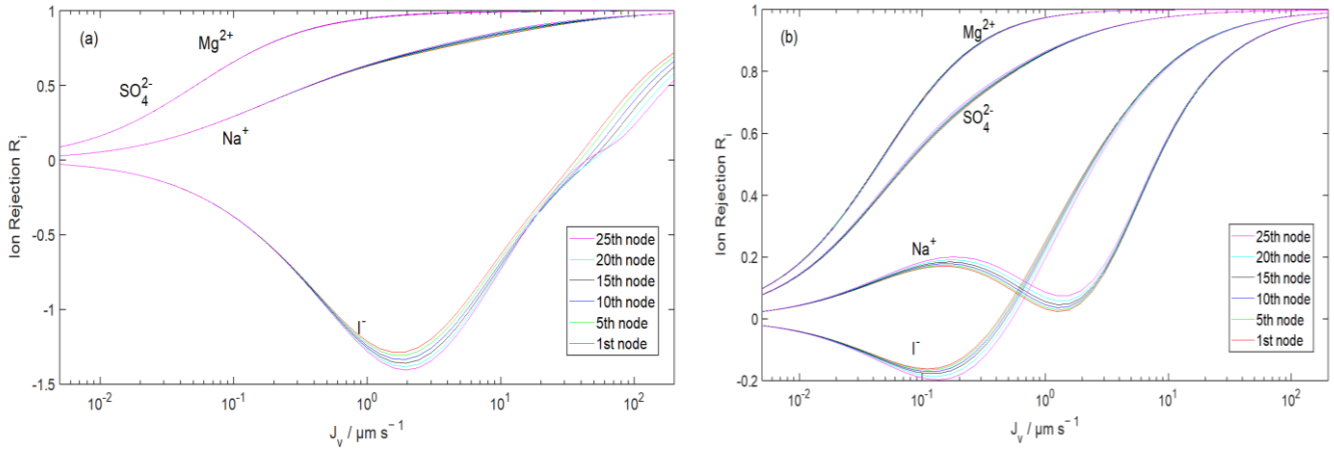


**Figure 9.** Case Study 2—Calculated relation between ion rejections and transmembrane permeate flux in selected membrane nodes in the first (**a**) and second (**b**) stage of the optimized membrane flowsheet (Figure 9). Parameters from Tables S6 and S7.

Explicit calculation of all relevant variables in each node and all collocation points allowed considering the respective contributions to the ion flux, which are shown in Figure 10. $Mg^{2+}$ is transported through the membrane by diffusion. In contrast, the electrostatic field with the negative potential in the direction of the permeate side decelerates the ion flux. Thus, the diffusive contribution increases along the membrane length due to the low permeance, causing an increased driving force (i.e., concentration gradient). In later nodes, the electromigration contribution for $Mg^{2+}$ transport also increases due to the increase in the gradient of the electrostatic potential. However, the increase in diffusion predominates, so that the ion flux in the posterior nodes increases. For $SO_4^{2-}$, this is different. Here, diffusion and electromigration act in the same direction. Similar to $Mg^{2+}$, the diffusion fraction across the node increases, resulting in an increasing ion flux, accompanied by an increase in the electrostatic potential. $Na^+$ ions behave similarly to $Mg^{2+}$ ions, so that the ion flux also increases in the posterior nodes. In contrast, the diffusion of iodide anions acts in the direction of the feed side, due to the negative rejection (i.e., the greater $I^-$ concentrations in the permeate). Electromigration exerts an attractive effect on iodide that prevails over diffusion and results in an approximately constant ion flux across all nodes.

### *3.3. Case Study 3—Application on Lithium Separation from Aqueous Sources*

While the first two case studies presented were based on hypothetical test systems, the third case study focuses on a real-system separation task. The growing demand for lithium in the electrical and automotive industries necessitates the exploration of new lithium sources. Seawater is an abundant reservoir of lithium; however, its concentration is extremely low, measuring at 0.21 ppm. Nanofiltration has proven to be effective in significantly reducing the ratio of divalent ions such as $Mg^{2+}$ and $Ca^{2+}$ to $Li^+$. In this study, a novel method was developed to optimize the plant layout, enabling high rejection of $Mg^{2+}$ while maintaining or even increasing the concentration of $Li^+$ in the membrane stages due to slightly negative rejection. Table S8 shows the parameters used for this case study. Aside from lithium, the most important cations in seawater are listed. The permeances were obtained by fitting to experimental data in one of our previous papers [31]. The rejection difference between $Mg^{2+}$ and $Li^+$ was chosen as the objective function to be maximized and the stage-cut was fixed to 0.25. Note that the variables in this case study are mass-based, according to the original experimental values.

The results of the flowsheet optimization are shown in Figure 11. The system converges in the first stage to an operating pressure of 35.73 bar, which decreases slightly by 0.01 bar in this membrane stage due to pressure loss in the module. The resulting membrane area of 30.92 $m^2$ provides the set stage cut of 0.25. Due to the high $Mg^{2+}$ rejection, a SF of 13.6 and a rejection difference of 0.93 was achieved in the first stage. As can be seen in Figure 12, the divalent ions $Ca^{2+}$ and $Mg^{2+}$ have significantly higher rejection for all permeate fluxes, while the monovalent cations initially have negative rejection for low permeate fluxes, which later changes to positive rejection. In the second stage, negative rejection of $Li^+$ is no longer achieved and the operating point shifts slightly to the left to a lower pressure of 12.66 bar. However, the permeate flux through the membrane remains largely unchanged, as the osmotic pressure in the feed has also decreased significantly in the second stage. In the third stage, the ratio of $Mg^{2+}$ to $Li^+$ can then be significantly reduced again to a mol-based ratio of 2.8.

Another possibility to further reduce this ratio would be to maximize the separation factor as a target function. However, this would result in very high residues and thus also considerably lower the concentration of $Li^+$ in the permeate. The computational time was 179 s with 1622 variables to be computed.

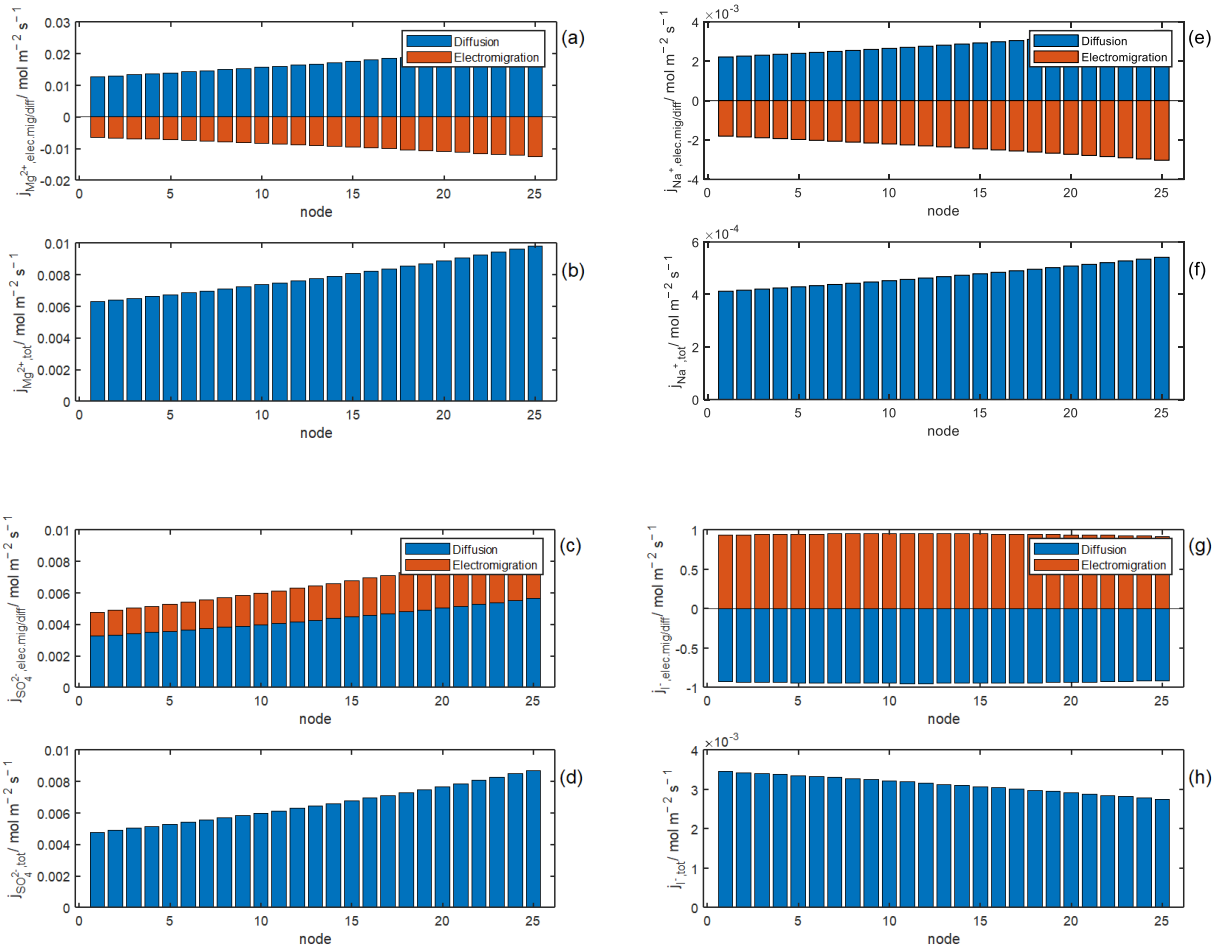


**Figure 10.** Contribution of diffusion (blue) and electromigration (orange) (Equation (1)) to the ion flux and total ion flux in the different membrane nodes in the first membrane stage of the optimized flowsheet of Case Study 2. Parameters are listed in Tables S6 and S7. (**a**,**b**) depicts the contributions and total ion flux for $Mg^{2+}$, (**c**,**d**) for $SO_4^{2-}$, (**e**,**f**) for $Na^+$, (**g**,**h**) for $I^-$.

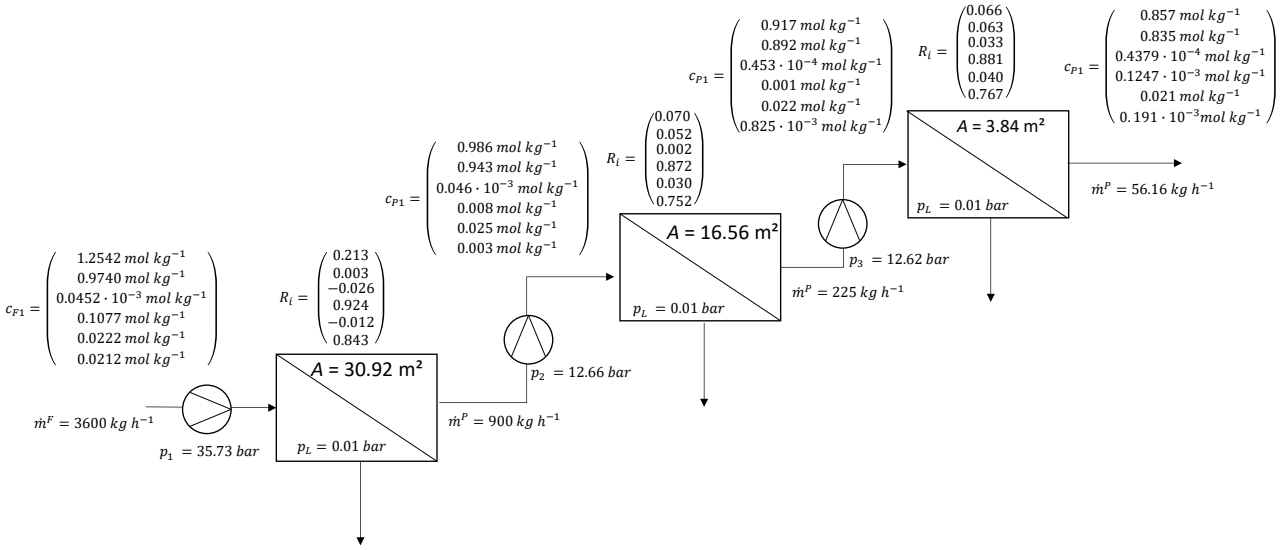


**Figure 11.** Optimized three-stage membrane flowsheet of case study 3 with optimized pump pressure in each stage including parameters of Tables S8 and S9. Ion concentrations and rejections in the $c_i$ and $R_i$ vector are in the order $Cl^-$, $Na^+$, $Li^+$, $Mg^{2+}$, $K^+$, $Ca^{2+}$.

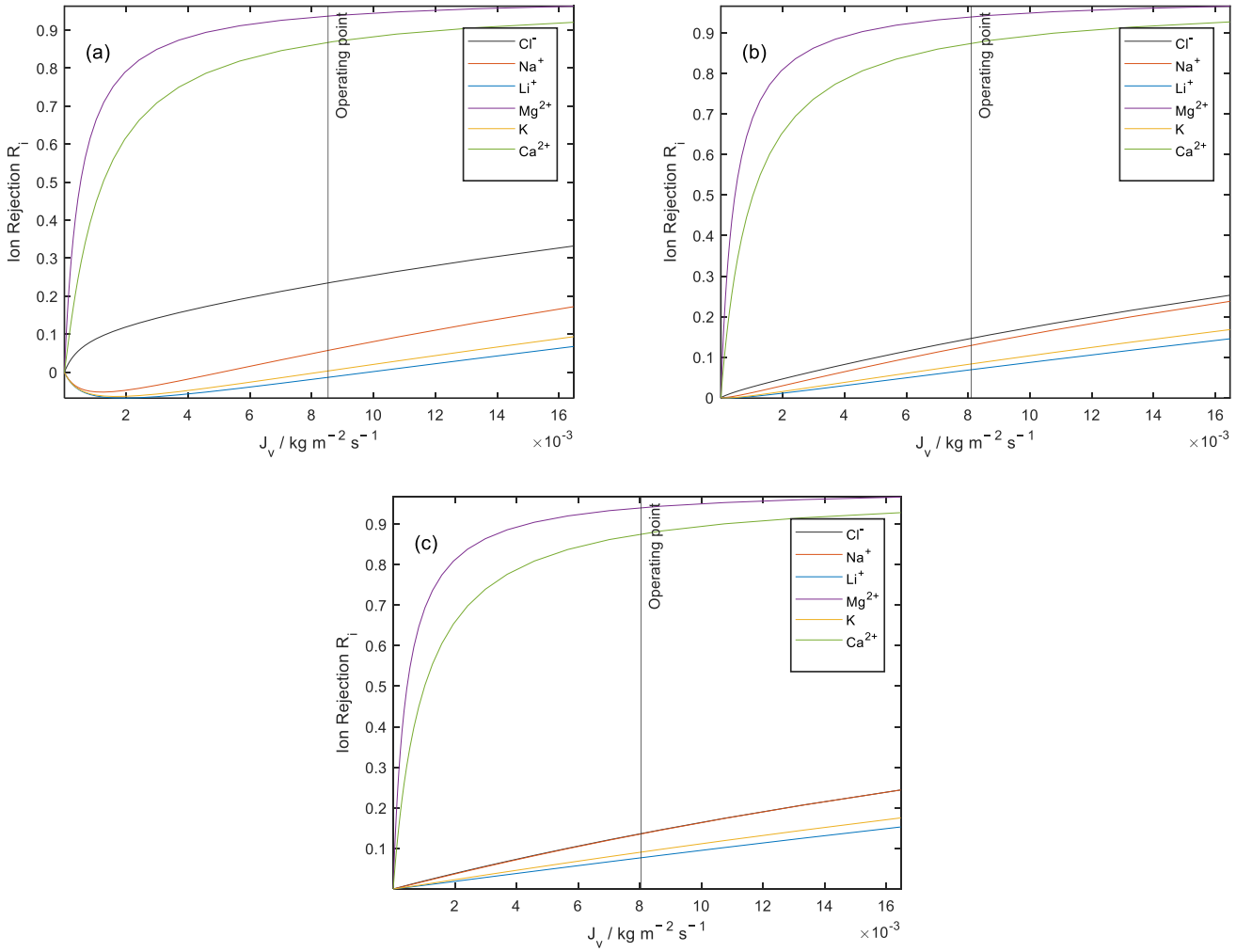


**Figure 12.** Calculated ion rejections of three membrane stages as a function of the total permeate flux calculated by the SDEM model and operating point at optimized pump pressure with parameters of Tables S8 and S9. (**a**) corresponds to the first node in the first membrane stage and (**b**,**c**) to the second and third membrane stage, respectively.

## 4. Conclusions

In this work, a method was developed to efficiently model predefined membrane interconnections with set variables using a discretization both along the membrane length and across the membrane thickness. All resulting differential equations were transformed into an algebraic system of equations, which can be solved by any non-linear programming solver. To the best of our knowledge, this is the first time that the solution-diffusion–electromigration model has been used as a transport model in a basic membrane flowsheet. In addition to simulating the process, the model was also used to optimize a given flowsheet where the objective function was flexibly set, in this case to maximize the difference in ion rejections and the minimization of the membrane. Apart from the problem specification, the initialization method only required the definition of the stage cut, thereby reducing the required inputs to a minimum. Additional constraints might be set (e.g., $c_{ions}$ < saturation limit).

The resulting detailed information about the multi-stage membrane process was used to investigate which transportation mechanism predominates for each ion. The introduced methodology was evaluated specifically for three different separations tasks, the separation of two anion species in the first case study using a hypothetical mixture of water and two salts, and the separation of an anion and a cation species in the second case study with real experimental data of an aqueous two-salt mixture. Furthermore, in a third case study with experimentally obtained permeances, it was shown how the presented method performs in

the design and optimization of a process for the separation of highly demanded lithium ions from divalent ions. Therefore, the number of total ion species in the system was different in the case studies. Depending on the ions' properties (i.e., charges, permeances, and feed concentrations), negative rejections were achieved for some ions, allowing for a favorable separation between these ions from the other ions. To exploit these relations, the optimal pressure was optimized by the model taking into account the osmotic pressure difference and the pressure losses within the membrane module.

To increase the applicability in industry, extensions of the model in terms of cost functions, osmotic pressure calculations for high concentrated solutions and optimization of the arrangement of membrane stages are desirable in the future. The method presented here offers the flexibility to integrate with an established robust flowsheet optimization approach, contributing to the ongoing trend of automated flowsheet generation through the utilization of artificial intelligence.

**Supplementary Materials:** The following supporting information can be downloaded at: https://www.mdpi.com/article/10.3390/pr11082355/s1. Supplementary Materials S1: Details on modeling and optimization, Figure S1: Flow of calculation algorithm. Table S1: List of variables. Table S2: Parameters used for case study 1 in Equations (1) and (5). Permeances (Equation (1)) of the artificial equimolar mixture of the dissolved salts MA and $M_2B$ are taken from Yaroshchuk and Bruening [14]. Table S3: Case Study 1—used parameters without optimization in modeling with constant pump pressure (8 bar) in Equations (S1), (S2), (S5), and (S6). Additional parameters are listed in Table S2. Table S4: Case Study 1—used parameters with optimization of the pump pressure in Equations (S1), (S2), (S5), and (S6). Additional parameters are listed in Table S2. Table S5: Experimental rejections of $MgSO_4$ and NaI used for case study 2 with NF270 (Dow Chemicals) at T = 23 ± 2 °C, transmembrane pressure difference 7–20 bar, and a cross-flow rate of 0.7 m $s^{-1}$ from Pages et al. [28]. Feed concentrations of 0.1 mol $L^{-1}$ $MgCl_2$ and 0.0005 mol $L^{-1}$ NaI. Table S6: Parameters used for case study 2 in Equations (1) and (5). Salt feed concentrations were taken from Pages et al. [28]. Permeances were regressed to the $MgSO_4$ + NaI experiment by Pages et al. [28] at transmembrane pressure 7–20 bar at cross-flow rate of 0.7 m $s^{-1}$ a, T = 23 ± 2 °C with NF270 membrane (Dow Chemicals), and feed concentrations of 0.1 mol L 1 $MgCl_2$ and 0.0005 mol $L^{-1}$ NaI. Table S7: Case Study 2—used parameters with optimization of the pump pressure in Equations (S1), (S2), (S5), and (S6). Additional parameters are listed in Table S6. Table S8: Parameters used for case study 3 in Equations (1) and (5). Permeances were regressed to five subsystems of the involved ions at transmembrane pressure 5–40 bar at cross-flow rate of 2.05 m $s^{-1}$, T = 20 °C with NFAL membrane (Alfa Laval), and AMem = 17 $cm^2$ [25]. Table S9: Case Study 3—used parameters with optimization of the pump pressure in Equations (S1), (S2), (S5), and (S6). Additional parameters are listed in Table S8.

**Author Contributions:** T.H.: Methodology, Software, Validation, Formal analysis, Investigation, Data curation, Writing—original draft preparation, Visualization. S.S.: Validation, Writing—review and editing, Supervision. C.H.: Resources, Supervision, Writing—review and editing, Project administration, Funding acquisition. All authors have read and agreed to the published version of the manuscript.

**Funding:** This research received no external funding.

**Data Availability Statement:** Data is contained within the article and Supplementary Materials.

**Acknowledgments:** We acknowledge financial support by Deutsche Forschungsgemeinschaft and Technische Universität Dortmund/TU Dortmund University within the funding programme Open Access Costs. University within the funding program Open Access Publishing.

**Conflicts of Interest:** The authors declare that they have no known competing financial interest or personal relationships that could have appeared to influence the work reported in this paper.

## Abbreviations

| | | |
|---|---|---|
| Latin letters | | |
| $\tilde{V}_{H_2O}$ | Molar volume | $m^3\ mol^{-1}$ |
| $c_i^{F,j}$ | Feed concentration of ion in node $j$ | $mol\ L^{-1}$ |
| $c_i^{P,j}$ | Permeate concentration of ion in node $j$ | $mol\ L^{-1}$ |
| $c_i^{R,j}$ | Retentate concentration of ion in node $j$ | $mol\ L^{-1}$ |
| $A_{ch}$ | Cross-sectional area of the membrane channel | $m^2$ |
| $A_p$ | Cross-sectional area of the pipe | $m^2$ |
| $A_{sh}$ | Cross-sectional area of the module's shell part | $m^2$ |
| $\dot{V}^{F,j}$ | Feed volume flow in node $j$ | $L\ min^{-1}$ |
| $\dot{V}^{P,j}$ | Permeate volume flow in node $j$ | $L\ min^{-1}$ |
| $\dot{V}^{R,j}$ | Retentate volume flow in node $j$ | $L\ min^{-1}$ |
| $J_v^j$ | Transmembrane volume flux in node $j$ | $m\ s^{-1}$ |
| $P_i$ | Permeance of ion $i$ | $\mu m\ s^{-1}$ |
| $Q_{H2O}$ | Saltwater permeability | $m\ s^{-1}\ bar^{-1}$ |
| $Z_i$ | Charge number of ion $i$ | - |
| $c_i$ | Concentration of ion $i$ | $mol\ L^{-1}$ |
| $d_{ch}$ | Diameter of membrane channel | m |
| $j_i$ | Transmembrane ion flux of ion $i$ | $mol\ m^{-2}\ s^{-1}$ |
| $l_{ch}$ | Length of membrane channel | m |
| $i$ | Component index | - |
| $k$ | Component index | - |
| $j$ | Node index | - |
| $n_t$ | Parallel tubes in membrane module | - |
| $p^F$ | Feed pressure supplied by pump | bar |
| $v_{j,ch}$ | Velocity in membrane channel in node $j$ | $m\ s^{-1}$ |
| $v_p$ | Velocity in pipe | $m\ s^{-1}$ |
| $F$ | Faraday constant | $C\ mol^{-1}$ |
| $f$ | Fanning friction factor | - |
| $n$ | Number of ion species | - |
| $N$ | Number of nodes | - |
| $R$ | Molar gas constant | $J\ K^{-1}\ mol^{-1}$ |
| $Re$ | Reynolds number | - |
| SDEM | Solution-diffusion–electromigration model | |
| SDM | Solution-diffusion model | |
| $T$ | Temperature | K |
| $v$ | Number of collocation points | - |
| $x$ | Transmembrane coordinate | m |
| $\Delta p_{f,j}$ | Pressure loss within the membrane channels | bar |
| $\Delta p_{in}$ | Pressure loss at the module inlet | bar |
| y | Arbitrary variables to demonstrate the method of collocation | - |
| z | Collocation point | - |
| Greek letters | | |
| $\rho$ | Saltwater density | $kg\ m^{-3}$ |
| $\alpha$ | Polynomial coefficients | - |
| $\delta$ | Membrane thickness | $\mu m$ |
| $\pi^{P,j}$ | Osmotic permeate pressure in node $j$ | bar |
| $\pi^{F,j}$ | Osmotic feed pressure in node $j$ | bar |
| $\phi$ | Dimensionless electrostatic potential in the virtual solution | - |

## References

1. Yu, L.-Y.; Wu, K.-J.; He, C.-H. A two-step green liquid-liquid extraction strategy for selective lithium recovery and application to seawater. *Hydrometallurgy* **2023**, *220*, 106102. [CrossRef]
2. Yang, S.; Zhang, F.; Ding, H.; He, P.; Zhou, H. Lithium Metal Extraction from Seawater. *Joule* **2018**, *2*, 1648–1651. [CrossRef]

3. Lee, M.; Jung, W.; Kwon, H.J.; Lim, G. Continuous ion separation via electrokinetic-driven ion migration path differentiation: Practical application to lithium extraction from brines. *J. Mater. Chem. A* **2022**, *10*, 4621–4633. [CrossRef]
4. Li, Z.; Li, C.; Liu, X.; Cao, L.; Li, P.; Wei, R.; Li, X.; Guo, D.; Huang, K.-W.; Lai, Z. Continuous electrical pumping membrane process for seawater lithium mining. *Energy Environ. Sci.* **2021**, *14*, 3152–3159. [CrossRef]
5. Xu, P.; Hong, J.; Qian, X.; Xu, Z.; Xia, H.; Tao, X.; Xu, Z.; Ni, Q.-Q. Materials for lithium recovery from salt lake brine. *J. Mater. Sci.* **2021**, *56*, 16–63. [CrossRef]
6. Liu, G.; Zhao, Z.; Ghahreman, A. Novel approaches for lithium extraction from salt-lake brines: A review. *Hydrometallurgy* **2019**, *187*, 81–100. [CrossRef]
7. Yaroshchuk, A.E. Dielectric exclusion of ions from membranes. *Adv. Colloid Interface Sci.* **2000**, *85*, 193–230. [CrossRef]
8. Ahmad, N.N.R.; Ang, W.L.; Teow, Y.H.; Mohammad, A.W.; Hilal, N. Nanofiltration membrane processes for water recycling, reuse and product recovery within various industries: A review. *J. Water Process Eng.* **2022**, *45*, 102478. [CrossRef]
9. Yaroshchuk, A. Non-steric mechanisms of nanofiltration: Superposition of Donnan and dielectric exclusion. *Sep. Purif. Technol.* **2001**, *22–23*, 143–158. [CrossRef]
10. Spiegler, K.S.; Kedem, O. Thermodynamics of hyperfiltration (reverse osmosis): Criteria for efficient membranes. *Desalination* **1966**, *1*, 311–326. [CrossRef]
11. Hussain, A.A.; Abashar, M.; Al-Mutaz, I.S. Effect of Ion Sizes on Separation Characteristics of Nanofiltration Membrane Systems. *J. King Saud Univ. Eng. Sci.* **2006**, *19*, 1–18. [CrossRef]
12. Bowen, W.; Welfoot, J.S. Modelling the performance of membrane nanofiltration—Critical assessment and model development. *Chem. Eng. Sci.* **2002**, *57*, 1121–1137. [CrossRef]
13. Bowen, W.; Mukhtar, H. Characterisation and prediction of separation performance of nanofiltration membranes. *J. Membr. Sci.* **1996**, *112*, 263–274. [CrossRef]
14. Ghorbani, A.; Bayati, B.; Drioli, E.; Macedonio, F.; Kikhavani, T.; Frappa, M. Modeling of Nanofiltration Process Using DSPM-DE Model for Purification of Amine Solution. *Membranes* **2021**, *11*, 230. [CrossRef]
15. Mohammad, A.W.; Hilal, N.; Al-Zoubi, H.; Darwish, N.A. Prediction of permeate fluxes and rejections of highly concentrated salts in nanofiltration membranes. *J. Membr. Sci.* **2007**, *289*, 40–50. [CrossRef]
16. Wang, R.; Lin, S. Pore model for nanofiltration: History, theoretical framework, key predictions, limitations, and prospects. *J. Membr. Sci.* **2021**, *620*, 118809. [CrossRef]
17. Bandini, S.; Boi, C. Transport phenomena in reverse osmosis/nanofiltration membranes. In *Current Trends and Future Developments on (Bio-) Membranes*; Elsevier: Amsterdam, The Netherlands, 2021; pp. 49–90.
18. Yaroshchuk, A.; Bruening, M.L.; Zholkovskiy, E. Modelling nanofiltration of electrolyte solutions. *Adv. Colloid Interface Sci.* **2019**, *268*, 39–63. [CrossRef]
19. Yaroshchuk, A.; Bruening, M.L. An analytical solution of the solution-diffusion-electromigration equations reproduces trends in ion rejections during nanofiltration of mixed electrolytes. *J. Membr. Sci.* **2017**, *523*, 361–372. [CrossRef]
20. Yaroshchuk, A.; Bruening, M.L.; Licón Bernal, E.E. Solution-Diffusion–Electro-Migration model and its uses for analysis of nanofiltration, pressure-retarded osmosis and forward osmosis in multi-ionic solutions. *J. Membr. Sci.* **2013**, *447*, 463–476. [CrossRef]
21. Fernández de Labastida, M.; Yaroshchuk, A. Nanofiltration of Multi-Ion Solutions: Quantitative Control of Concentration Polarization and Interpretation by Solution-Diffusion-Electro-Migration Model. *Membranes* **2021**, *11*, 272. [CrossRef]
22. López, J.; Yaroshchuk, A.; Reig, M.; Gibert, O.; Cortina, J.L. An engineering model for solute transport in semi-aromatic polymeric nanofiltration membranes: Extension of Solution-Electro-Diffusion model to complex mixtures. *J. Environ. Chem. Eng.* **2021**, *9*, 105262. [CrossRef]
23. Du, Y.; Xie, L.; Liu, J.; Wang, Y.; Xu, Y.; Wang, S. Multi-objective optimization of reverse osmosis networks by lexicographic optimization and augmented epsilon constraint method. *Desalination* **2014**, *333*, 66–81. [CrossRef]
24. Skiborowski, M.; Mhamdi, A.; Kraemer, K.; Marquardt, W. Model-based structural optimization of seawater desalination plants. *Desalination* **2012**, *292*, 30–44. [CrossRef]
25. Kotb, H.; Amer, E.H.; Ibrahim, K.A. On the optimization of RO (Reverse Osmosis) system arrangements and their operating conditions. *Energy* **2016**, *103*, 127–150. [CrossRef]
26. Garg, M.C.; Joshi, H. Optimization and economic analysis for a small scale nanofiltration and reverse osmosis water desalination system. *Water Supply* **2015**, *15*, 1027–1033. [CrossRef]
27. Alves, Y.P.C.; Antunes, F.A.F.; Da Silva, S.S.; Forte, M.B.S. From by- to bioproducts: Selection of a nanofiltration membrane for biotechnological xylitol purification and process optimization. *Food Bioprod. Process.* **2021**, *125*, 79–90. [CrossRef]
28. Geraldes, V.; Brites Alves, A.M. Computer program for simulation of mass transport in nanofiltration membranes. *J. Membr. Sci.* **2008**, *321*, 172–182. [CrossRef]
29. Roy, Y.; Sharqawy, M.H.; Lienhard, J.H. Modeling of flat-sheet and spiral-wound nanofiltration configurations and its application in seawater nanofiltration. *J. Membr. Sci.* **2015**, *493*, 360–372. [CrossRef]
30. Fridman-Bishop, N.; Nir, O.; Lahav, O.; Freger, V. Predicting the Rejection of Major Seawater Ions by Spiral-Wound Nanofiltration Membranes. *Environ. Sci. Technol.* **2015**, *49*, 8631–8638. [CrossRef]

31. Hubach, T.; Schlüter, S.; Held, C. $Li^+$ separation from aqueous sources by nanofiltration membranes: Experiments and modeling: Submitted. *J. Membr. Sci.* **2023**.
32. Pagès, N.; Reig, M.; Gibert, O.; Cortina, J.L. Trace ions rejection tunning in NF by selecting solution composition: Ion permeances estimation. *Chem. Eng. J.* **2017**, *308*, 126–134. [CrossRef]